LAWRENCE
LIVERMORE
NATIONAL
LABORATORY

UCRL-JRNL-220083

Reynolds number effects on Rayleigh-Taylor Instability with Implications for Type Ia Supernovae

W. H. Cabot, A. W. Cook

March 23, 2006

Science Journal

Disclaimer

Reynolds number effects on Rayleigh-Taylor Instability with Implications for Type Ia Supernovae

William H. Cabot and Andrew W. Cook

Lawrence Livermore National Laboratory,
7000 East Ave., Livermore, CA 94550-9234, USA

Spontaneous mixing of materials at unstably stratified interfaces occurs in a wide variety of atmospheric, oceanic, geophysical and astrophysical flows. The Rayleigh-Taylor instability, in particular, plays key roles in the death of stars, planet formation and the quest for controlled thermonuclear fusion. Despite its ubiquity, fundamental questions regarding Rayleigh-Taylor instability persist. Among such questions are: Does the flow forget its initial conditions? Is the flow self-similar? What is the value of the scaling constant? How does mixing influence the growth rate? Here we show results from a 3072^3 grid-point Direct Numerical Simulation in an attempt to answer these and other questions. The data indicate that the scaling constant cannot be found by fitting a curve to the width of the mixing region (as is common practice) but can only be accurately obtained by recourse to the similarity equation for the growth rate. The data further establish that the ratio of kinetic energy to released potential energy is not constant, as has heretofore been assumed. The simulated flow reaches a Reynolds number of 32,000, far exceeding that of all previous simulations. The latter stages of the simulation reveal a weak Reynolds number dependence, which may have profound consequences for modeling Type Ia supernovae as well as other high Reynolds number flows.

Rayleigh-Taylor (R-T) instability is the baroclinic generation of vorticity at a perturbed interface subject to acceleration in a direction opposite the mean density gradient [1, 2, 3]. Alternatively, it is the dynamic process by which two fluids seek coexistence at a lower energy state. It occurs at very large scales; e.g., interstellar gas, pushed out of the galactic plane by magnetic fields and cosmic rays, becomes R-T unstable if driven beyond its natural scale height [4]. It also occurs at very small scales; e.g., snapping shrimp, which produce most of the ambient noise in subtropical shallow waters throughout the world, produce their sound through collapse of a cavitation bubble, generated by a water jet formed from rapid claw closure; the bubble is destroyed through a Rayleigh-Taylor instability [5].

The tendency of R-T instability to generate both large and small scales has far-reaching consequences for impact-driven accretion of planets. Heavy metal asteroids and planetesimals, upon striking a lighter silicate crust, fragment via R-T instability. The size distribution of the resulting chunks then determines how much of the incoming iron-rich material equilibrates isotopically with the silicate layer and how much aggregates back together into larger agglomerations, which then migrate, via another R-T instability, toward the core [6, 7]. Accretion via large-scale collisions is thought to be responsible for 99% of the Earth's growth; hence, R-T unstable asteroids have had a profound impact on our planet.

R-T instability plays a crucial role in all major forms of fusion, whether confinement be magnetic [8], inertial [9] or gravitational [10]. It is even thought to play a role limiting the driving pressure in the violent collapse of acoustically forced bubbles in sonoluminescence and "sonofusion" phenomena [11, 12]. In regard to gravitational fusion, much work over recent years points to R-T instability as the dominant acceleration mechanism for thermonuclear flames in Type Ia supernovae [13]. Estimates for the rate of cosmological expansion depend critically on the variability in luminosity of these events. Hence, an improved understanding of R-T physics is required to more accurately predict the fate of the universe.

Governing equations and their solution

Rayleigh-Taylor instability is a low Mach number phenomenon [14]; hence, for this study, we chose an incompressible formulation of the governing equations in order to avoid the complicating effect of hydrostatic density variation in the stratified layers. The governing equations for two incompressible miscible fluids in an accelerating frame of reference are [15]:

$$\frac{\partial \rho}{\partial t} + u_j \frac{\partial \rho}{\partial x_j} = -\rho \frac{\partial u_j}{\partial x_j} = \rho \frac{\partial}{\partial x_j} \left(\frac{D}{\rho} \frac{\partial \rho}{\partial x_j} \right) , \tag{1}$$

$$\frac{\partial \rho u_i}{\partial t} + \frac{\partial \rho u_i u_j}{\partial x_j} = \rho g_i - \frac{\partial p}{\partial x_i} + \frac{\partial \tau_{ij}}{\partial x_j} , \tag{2}$$

where

$$\tau_{ij} = \mu \left[\frac{\partial u_i}{\partial x_j} + \frac{\partial u_j}{\partial x_i} - \frac{2}{3} \delta_{ij} \frac{\partial u_k}{\partial x_k} \right] .$$

Here t is time, $x_j = (x, y, z)$ is distance, ρ is density, $u_i = (u, v, w)$ is velocity, p is pressure, $g_i = (0, 0, -g)$ is acceleration, D is mass diffusivity, μ is shear viscosity, and τ_{ij} is the viscous stress tensor.

The equations are solved using a hybrid spectral-Padé scheme for spatial derivatives, combined with a pressure-projection method for temporal integration. The scheme is designed to minimize numerical dissipation, while maximizing the range of scales that are well resolved by the discrete derivatives. Verification and validation tests of the numerical algorithm have previously been reported [15, 16]. The solution constitutes a Direct Numerical Simulation (DNS) in the sense that all scales of motion, including the viscous and diffusive scales, are completely resolved; i.e., energy dissipation is physical rather than numerical.

The R-T flow was initialized in a quiescent state, with heavy fluid of density ρ_H placed atop light fluid of density ρ_L, where $\rho_H / \rho_L = 3$, corresponding to an Atwood number

$$A \equiv \frac{\rho_H - \rho_L}{\rho_H + \rho_L} \tag{3}$$

of 1/2. At the interface ($z = 0$), a thin diffusion zone spanning roughly 6 grid points was created with fine-scale perturbations fit to a Gaussian spectrum peaked at mode 96 (32 points per wavelength). In the simulation, the grid spacing was uniform ($\Delta = \Delta x = \Delta y = \Delta z$); gravity ($g$), diffusivity ($D$), and kinematic viscosity ($\nu = \mu/\rho$) were set to constant values, with the grid Grashof number ($2gA\Delta^3/\nu^2$) and the Schmidt number (ν/D) both equal to unity. The DNS was performed on a $3072 \times 3072 \times N_z$ vertically expanding grid with periodic boundaries in x and y. At the beginning of the simulation, N_z was 256; by the end, N_z reached a value of 3072, forming a cubic domain. At earlier stages, a potential flow solution, with impermeable free-slip conditions at the top and bottom of the final cube, was matched to the intermediate z boundaries. Tests of the z boundary condition were performed on domains with different aspect ratios to ensure the matching procedure had no artificial influence on the flow. The simulation ran for just over two weeks on the IBM BlueGene/L machine, first utilizing 4.3 days on 32,768 nodes (half machine) and then consuming 10.2 days on 65,536 nodes (full machine).

Figure 1 shows the mixing region near the end of the simulation. Not shown are the pure fluids above and below the mixing region. One item to note from the graphic is that very little pure fluid makes it across the middle of the mixing region and almost none reaches all the way through to the other side; viz., there is no red fluid at the very bottom. This picture is qualitatively consistent with Type Ia supernova spectra, which imply that unburnt materials are not transported to the center of the star; i.e., Doppler shifts show unburnt carbon and oxygen only at high velocities associated with expanding outer layers [17].

Characteristic length and time scales

Relevant length and times scales for the flow are set by gravity and the initial perturbations. A characteristic horizontal wavelength of any variable, $\phi(x, y, z, t)$, is

$$l_\phi(t) \equiv 2\pi \frac{\int_0^{k_{\max}} E_\phi(k, 0, t)/k \; dk}{\int_0^{k_{\max}} E_\phi(k, 0, t) \; dk} \; , \tag{4}$$

where $k = \sqrt{k_x^2 + k_y^2}$ is the magnitude of horizontal wavevectors associated with an annulus in Fourier space, $k_{\max} = \pi/\Delta$, corresponding to a maximum mode number of 1536, and $E_\phi(k, z, t)$ is the two-dimensional energy spectrum of ϕ fluctuations. The dominant initial wavelength is $l_o = l_\rho(0)$; therefore, a natural time scale is

$$\tau \equiv \left(\frac{l_o}{Ag} \right)^{1/2} \; . \tag{5}$$

For this simulation, $l_o = 32\Delta$ and $\tau = 8\sqrt{\Delta/g}$.

In the linear regime (for small amplitude perturbations), the exponential growth rate factor for R-T instability is $\sqrt{gAk}$ when there is no viscosity or mass diffusion. Finite viscosity inhibits high-wavenumber growth, producing a "most dangerous" mode corresponding to the maximum growth rate. Finite diffusion actually stabilizes the flow above a critical wavenumber k_D. By including viscous/diffusive effects, the growth factor for the linear regime was found by Duff et al. [18] to be

$$n = \left(gAk/\psi + \nu^2 k^4 \right)^{1/2} - (\nu + D)k^2 \; , \tag{6}$$

where ψ is a function of A, k and the initial thickness of the diffuse density layer, δ. For our choice of $A = 1/2$, they found $\psi \approx 1 + 0.375k\delta$. With an initial layer thickness of $\delta \approx 6\Delta$ and the other run parameters given above, we find from (6) that the most rapidly growing perturbation occurs at mode number 74 (wavelength $\approx 41\Delta$), and that mode numbers greater than 214 are stabilized (wavelengths $< 14\Delta$). Note that conductive propagation of the laminar flame in reacting flow acts to suppress small-scale density fluctuations and stabilizes

the R-T instability in a manner roughly analogous to the mass diffusion. Timmes and Woosley [19] estimated that wavenumbers greater than gA/S_l^2 are stabilized by the flame in the linear regime, where S_l is the laminar flame speed. For low Schmidt numbers ($\nu \ll D$) and thin interfaces ($\psi \approx 1$), (6) gives a similar result, assuming a correspondence between S_l and $Dk_D = (gAD)^{1/3}$. In the turbulent regime, flames interact with eddies of size greater than the Gibson scale, $l(S_l/u')^3$, where u' is the turbulent velocity intensity and l is the inertial length scale from (4) [20]. We expect that simulations of nonreacting R-T instability (presented here) and simulations of the reacting case (e.g., [13]) will exhibit similar behavior provided most of the turbulent energy resides at scales much larger than the diffusive or flame stabilization scales.

As the R-T-unstable flow evolves, the initial Gaussian spectrum of perturbations grows and broadens, eventually developing an inertial range. Figure 2 displays density and velocity spectra at the end of the simulation. The dominant wavelength, $l_\phi(t)$, of each variable approximately corresponds to the the peak of its spectrum. As time progresses, the peak of each spectrum moves to lower wavenumbers, whereas the tail (dissipation range) moves to higher wavenumbers. Hence, the range of scales participating in the dynamics grows at both ends. The flow Reynolds number ($Re \equiv H\dot{H}/\nu$ for some measure of mixing layer width H) provides another characterization of this range of scales, as well as a means for comparing simulations and experiments. A wide variety of turbulent flows have been observed to reach their asymptotic state only for $Re > 10,000$, which also corresponds to the appearance of an inertial range in the energy spectrum [21]. If we use the common definition of H as the vertical extent of the mixing region where the horizontal mean concentration of heavy fluid is between 1% and 99%, the Reynolds number for this DNS reaches a value of 32,000 (see Fig. 3), far exceeding all previously reported values [15, 22, 23] and crossing the 10,000 threshold for strong turbulence.

The rate of growth of the mixing layer at late time can be robustly defined in terms of

entrainment and mixing of pure fluid mole fractions. The mole fraction of heavy fluid is

$$X = \frac{\rho - \rho_L}{\rho_H - \rho_L} \,, \tag{7}$$

and the mole fraction of mixed fluid is

$$X_m(X) = \begin{cases} 2X & \text{if } X \leq 1/2 \\ 2(1-X) & \text{if } X > 1/2 \end{cases} \,. \tag{8}$$

With homogeneity in x and y, ensemble averages (denoted by angle brackets) are equivalent to horizontal integrals, i.e., for any variable $\phi(x, y, z, t)$ in a box with $L \times L$ horizontal dimensions,

$$\langle \phi \rangle (z, t) = \frac{1}{L^2} \int_0^L \int_0^L \phi(x, y, z, t) \, dx \, dy \,. \tag{9}$$

The width of the mixing region is defined as the thickness of mixed fluid that would result if the entrained fluids were perfectly homogenized in x and y, i.e.,

$$h \equiv \int_{-\infty}^{\infty} X_m(\langle X \rangle) \, dz \,. \tag{10}$$

Thus, h is an entrainment length derived from the volumes of pure fluids entering the turbulent mixing region. The visual width H, based in the 1% concentration threshold of the heavy fluid ($0.01 \leq \langle X \rangle \leq 0.99$), is observed to be about $2.4h$.

Turbulence length scales and the approach to isotropy

There is a large degree of anisotropy at large scales in this flow, as evident in the spectra in Fig. 2. It is therefore necessary to account for this anisotropy in defining turbulence length scales. A Taylor microscale in the ith direction can be defined as

$$\lambda_i(z, t) = \left[\frac{\langle u_i^2 \rangle}{\left\langle (\partial u_i / \partial x_i)^2 \right\rangle} \right]^{1/2} \quad \text{(no sum on } i\text{)} \,. \tag{11}$$

Similarly, a Kolmogorov scale in the ith direction can be defined as

$$\eta_i(z, t) = \left(\frac{\nu^3}{\epsilon_i} \right)^{1/4} \,, \tag{12}$$

where

$$\epsilon_i(z,t) = 15\nu \left\langle \left(\frac{\partial u_i}{\partial x_i} \right)^2 \right\rangle \quad \text{(no sum on } i\text{)} \tag{13}$$

is the dissipation rate. For isotropic turbulence,

$$\epsilon_i = \epsilon \equiv 2\nu S_{ij} S_{ij} \ , \tag{14}$$

where

$$S_{ij} = \frac{1}{2} \left(\frac{\partial u_i}{\partial x_j} + \frac{\partial u_j}{\partial x_i} \right) \tag{15}$$

is the strain rate tensor [24]. With horizontal isotropy, it is also convenient to combine x and y components, viz., $\lambda_{xy} = (\lambda_x + \lambda_y)/2$ and $\eta_{xy} = (\eta_x + \eta_y)/2$. The Taylor microscale is the "smallest large scale" and is associated with the interfacial surface area between the fluids (as will be shown). The Kolmogorov scale is the smallest turbulence length scale and is associated with viscous dissipation of kinetic energy; in the DNS we observe $\eta_i \approx \Delta$ at late times.

The moment similarity method of Ristorcelli and Clark [23] predicts $\lambda_i \propto h^{1/4} \propto t^{1/2}$ and $\eta_i \propto h^{-1/8} \propto t^{-1/4}$. We have tested these predictions and plot the results in Fig. 4. Our results confirm the similarity predictions for η_{xy}, η_z and λ_{xy}, but not for λ_z. Ristorcelli and Clark studied Boussinesq ($A \ll 1$) flow where the anisotropy can be neglected. In the non-Boussinesq case, the anisotropic body force is felt at the Taylor microscale, but its effect becomes completely lost at the Kolmogorov scale. This fits well with the classical picture of turbulence, that small scales are more isotropic than large scales. Zingale et al. [13] found a similar small-scale tendency towards isotropy in their simulations of R-T unstable thermonuclear flames. This isotropy however, can take a very long time to develop, as demonstrated in Fig. 5, which shows the ratio of vertical to horizontal vorticity components in the central portion of the mixing layer. While the leading fronts of the mixing layer remain anisotropic for all time, the vorticity field behind the fronts evolves from a completely anisotropic state to completely isotropic state. The

isotropic state, however, is only obtained for $t/\tau > 27$ or $Re > 22,000$, which has never before been reached in a numerical simulation.

Growth rate

Recently, Ristorcelli and Clark [23] and Cook, Cabot and Miller [16], using completely different approaches, derived the same governing equation for h, namely,

$$\dot{h}^2 = 4\alpha A g h \ , \tag{16}$$

where α is an unknown growth parameter. In deriving (16), Ristorcelli and Clark employed a similarity assumption, whereas Cook et al. used a mass flux argument. In the Ristorcelli and Clark derivation, (16) results directly from the single assumption that solutions to the moment equations can be expressed as the product of a temporal scaling function and a spatial similarity function. If α is assumed constant, then the solution to (16) is (taking only the positive root as physically realizable)

$$h(t) = \alpha A g t^2 + 2(\alpha A g h_o)^{1/2} t + h_o \ , \tag{17}$$

where h_o is a virtual starting thickness, which depends on how long it takes for the flow to become self-similar, which in turn depends on the spectrum of initial perturbations. Alternatively, if one takes $t = 0$ in (17) to be the time when the flow first achieves self-similarity, then h_o corresponds to the thickness of the mixing region at that point.

Numerous attempts to measure α have been made by plotting h vs. Agt^2 and fitting a line to the most visually pleasing portion of the data. Dimonte et al. [25, 26] provide a history of such attempts and note that as grid resolutions have increased, α has decreased. More grid points enable simulations to run further in time, as measured by the number of "bubble merger generations": $l_\phi(t)/l_\phi(0) \propto h(t)/l_o$. The availability of more powerful computers has led to a somewhat ironic state of affairs, in that agreement between simulations and experiments is

worse today than it was several decades ago. Dimonte et al. and Ramabrabhu et al. [27] attribute the growing disparity to long wavelength modes in the experiments, which are not present in the more recent simulations. While this is almost certainly true, there is a more fundamental reason for the decrease in α from the simulations. Dividing (17) by Agt^2 gives

$$\alpha = \frac{h}{Agt^2} - \left(\frac{\alpha h_o}{Ag}\right)^{1/2} \frac{2}{t} - \frac{h_o}{Agt^2} \ . \tag{18}$$

Figure 6 compares α computed directly from (16) and from (18) by neglecting the last two terms. The former method yields a nearly constant value early in the simulation, whereas the latter method suffers from the t^{-1} dependence of the missing terms. The two measures have not come into agreement even by the end of the simulation. The top curve in the figure illustrates why larger simulations have generated lower values of α. Fitting a line to h vs. Agt^2 essentially picks off an α from the top curve corresponding to a time near the end of the simulation. R-T growth exhibits linear as well as quadratic behavior and the spectrum of initial perturbations determines the persistence of the linear term.

A close examination of the lower curve in Fig. 6 reveals that α is slightly increasing for $t/\tau > 20$, when Re is crossing 10,000. It is tempting to ignore this small effect or attribute it to statistical noise; however, there is a compelling reason why α may indeed exhibit a weak Reynolds number dependence, even in the fully self-similar regime. The reason relates to the energy budget and mixing dynamics.

Energy budget

The bandwidth of energy-containing scales in the flow grows like $h/\eta \propto t^{9/4}$ [23]. The potential energy released into the flow is

$$\delta P(t) = \int_V [\rho(\mathbf{x}, 0) - \rho(\mathbf{x}, t)] g z \, dV \ , \tag{19}$$

where $V = L^3$ is the volume of the full computational domain and $dV = dx\,dy\,dz$. The kinetic energy present in the flow is $K(t) = K_{xy}(t) + K_z(t)$, where

$$K_{xy}(t) = \frac{1}{2}\int_V \rho[u^2 + v^2]\,dV \tag{20}$$

and

$$K_z(t) = \frac{1}{2}\int_V \rho w^2\,dV\ . \tag{21}$$

Ratios of kinetic energy to released potential energy and horizontal energy to vertical energy are plotted in Fig. 7. The $K/\delta P$ ratio exhibits a shallow but steady rise for $t/\tau > 20$ or $Re > 10,000$. The Alpha Group [25] demonstrated that $\alpha \propto K/\delta P$ and report a constant value of $K/\delta P = 0.46 \pm 0.04$ from their numerical simulations. The Alpha-Group simulations were conducted at grid resolutions up to $256 \times 256 \times 512$ points. Simulations at that resolution are able to reach $h/l_o \approx 8$ or $t/\tau \approx 13$ before the flow feels the periodic boundaries [15, 16]. It is perhaps an unfortunate coincidence, that at this time the $K/\delta P$ ratio appears nearly flat.

The rise in $K/\delta P$ can be understood by examining the mechanical energy equation. Taking the dot product of velocity with the momentum equation (2), and dropping the negligible volume-expansion work term, $p\,\partial u_i/\partial x_i$, yields

$$\frac{\partial}{\partial t}\left(\frac{1}{2}\rho u_i u_i\right) + \frac{\partial}{\partial x_j}\left(\frac{1}{2}\rho u_i u_i u_j + p u_j - u_i \tau_{ij}\right) = -\rho g w - \tau_{ij}\frac{\partial u_i}{\partial x_j}\ . \tag{22}$$

Because there is no net flux through the boundaries, integrating (22) over the domain volume removes all the pure divergence terms on the l.h.s., resulting in

$$\frac{dK}{dt} = -\int_V \rho g w\,dV - \int_V \tau_{ij}\frac{\partial u_i}{\partial x_j}\,dV\ . \tag{23}$$

Substituting $\tau_{ij} = 2\rho\nu S_{ij}$ and decomposing $\partial u_j/\partial x_i$ into symmetric and anti-symmetric parts yields

$$\tau_{ij}\frac{\partial u_j}{\partial x_i} = 2\rho\nu S_{ij}S_{ij} = \rho\epsilon\ . \tag{24}$$

Furthermore, using

$$w \equiv \frac{Dz}{Dt} \equiv \left(\frac{\partial}{\partial t} + u_j \frac{\partial}{\partial x_j} \right) z \tag{25}$$

and

$$\int_V \rho g \frac{Dz}{Dt} \, dV = \frac{d}{dt} \int_V \rho g z \, dV \tag{26}$$

allows us to write (23) as

$$\frac{dK}{dt} = -\frac{d}{dt} \int_V \rho g z \, dV - \int_V \rho \epsilon \, dV \ . \tag{27}$$

Integrating (27) from 0 to t, and noting that the boundaries of the domain are fixed in time, results in

$$K(t) = \delta P(t) - \Psi(t) \ , \tag{28}$$

where $\delta P(t)$ is the total production given by (19), and $\Psi(t)$ is the total dissipation given by

$$\Psi(t) = \int_0^t \int_V \rho \epsilon \, dV \, dt' \ . \tag{29}$$

By inserting a self-similar form for $\langle \rho \rangle$ into (19), it can be shown that $\delta P \propto h^2$ [25]. We have normalized (28) by h^2 and plotted the three terms in Fig. 8. Energy production does indeed follow h^2 scaling; however, kinetic energy and dissipation do not. Dissipation lags production in a manner which causes K to grow faster than h^2. Potential energy is released into the layer at scales $\sim h$ and dissipated into heat at scales $\sim \eta$. As the separation between h and η increases, so too does the cascade time. The non-stationarity of the turbulent cascade is such that most of the kinetic energy present in the layer is that which has been most recently deposited. It takes roughly an eddy turnover time $\sim K/\dot{\Psi}$ for Ψ to respond to the energy deposited by δP; during this time, more energy is deposited than previously existed[1]. Virtually all R-T growth models assume $K/\delta P \propto \alpha =$ constant. If the rise in $K/\delta P$ persists beyond the window of this

[1]The energy dilemma is analogous to the cosmological expansion: to wit, we can't see the universe as it exists today, but only how it was in the far past.

simulation, there may be serious consequences for models of supernovae and other flows with Reynolds numbers that are many orders of magnitude higher. The effective Reynolds number (real or numerical) of any simulation is limited by grid resolution. Simulations and experiments at low Reynolds number might seriously underestimate the kinetic energy content of very high Reynolds number flows.

Mixing effects

The non-constant nature of $K/\delta P$ has a subtle effect on the mixing rate. The state of mixing within the layer can be quantified as the ratio of a mixing length to an entrainment length,

$$\Xi \equiv \frac{\int_{-\infty}^{\infty} \langle X_m \rangle \, dz}{h} \, . \tag{30}$$

Hence, Ξ will be unity for completely homogenized fluids and zero for completely segregated (entrained but undiffused) fluids. Figure 9 displays Ξ as a function of time. There is a shallow but persistent drop-off for $t/\tau > 20$. As the flow evolves, it entrains pure fluids in ever larger parcels and mixes them at ever finer scales. The turbulent cascade gets longer with increasing Reynolds number and pure fluids spend more time inside the layer before they get mixed. Pure fluids exert greater buoyancy forces than mixed fluids; hence, the growth rate increases as the stabilizing effect of mixing decreases.

Mixing also limits the rate of growth of the interfacial surface area between the two fluids. Figure 10 plots a_s/L^2 versus time, where a_s is the area of the equimolar ($X = 1/2$) isosurface and L^2 is the horizontal area of the computational domain. Once again, a change in slope is observed around $t/\tau = 20$ or $Re = 10,000$. Also shown in the figure is the interfacial surface area normalized by the square of the Taylor microscale ($\lambda_i \lambda_i$). The Taylor microscale normalization is flat because this is the length scale associated with wrinkling of the interfacial isosurface. Although the dependence of surface area and other flow properties on Reynolds

number is weak, the net effect may become large when extrapolated to Reynolds numbers many orders of magnitude higher than the DNS.

Astrophysical implications

The dependence of interfacial surface area on Reynolds number has important implications for Type Ia supernovae, where $Re \sim 10^{14}$ [28]. In addition to producing many intermediate-mass elements, Type Ia supernovae serve as standard candles for measuring the rate of expansion of the universe. They begin as carbon-oxygen white dwarfs, which accrete mass from a companion star. When the mass of the white dwarf reaches the Chandresekhar limit of 1.4 solar masses, ignition occurs near the center, which generates a thermonuclear flame front. Expansion of ashes behind the front causes the flame to become R-T unstable as it propagates outward. R-T wrinkling of the flame greatly increases the net burning rate, which depends on the laminar flame speed and the flame surface area [29, 17]. The thermonuclear flame varies in thickness, from 10^{-4} cm (the Kolmogorov scale) to ~ 1 cm [30, 31]. The radius of a white dwarf is $\sim 10^8$ cm; hence, DNS of the explosion would require a grid spanning 12 orders of magnitude in scale. In modern adaptive mesh refinement simulations, the numerical flame thickness is $\sim 10^6$ cm, taking account of resolution limitations [17]. We are therefore forced to utilized subgrid-scale models for unresolved physics for the foreseeable future.

The reaction rate and heat release terms in any given volume are proportional to $S_l a_s$, where S_l is the laminar flame speed and a_s is the flame's surface area. The actual surface area will greatly exceed the cross-sectional area L^2 when the flame is highly wrinkled. In typical Large Eddy Simulations (LES), a_s is grossly underrepresented; hence, $S_l a_s$ is replaced by $S_t L^2$, where S_t is an effectve turbulent flame speed provided by a subgrid-scale model. In strongly turbulent flows, $S_t \sim u'$, where u' is independent of S_l [32]. For reacting flow,

$$S_t/S_l = a_s/L^2 \; ; \tag{31}$$

hence, the area ratio in Fig. 10 mirrors the turbulent to laminar flame speed ratio [20].

A successful model for S_t in Type Ia supernovae must: a) produce enough energy to unbind the star, b) create observed amounts of intermediate-mass elements and c) eject materials with velocities matching Doppler shifts of spectral line emissions. Initial burning must be slow, to pre-expand the star, but then become fast, to produce large amounts of high-velocity intermediate-mass elements. To meet all these conditions, the turbulent flame must accelerate from S_l to roughly 30% of the speed of sound [33]. This final speed approximately corresponds to the maximum Mach number that a compressible R-T instability will produce [14]. Therefore, it seems prudent to ensure that the subgrid-scale model for S_t faithfully reproduces the physics of R-T instability before invoking other schemes to increase the burning rate, such as multi-point ignition, background turbulence from thermal convection and/or deflagration-to-detonation transition [33, 17].

In formulating a model for S_t, it is essential to realize that R-T instability grows up from small scales, as seen in the dispersion relation (6) from linear stability theory. In the early part of an LES, growth of R-T perturbations occurs far below the grid scale. Turbulence models that rely solely on a cascade from resolved-scale dynamics cannot hope to correctly capture R-T-driven combustion arising from subgrid scales. The results presented in this paper suggest that a reasonable model for S_t could be

$$S_t = S_{LD} + \dot{h} \ , \tag{32}$$

where $S_{LD} \approx 1.3 S_l$ is the speed of a thermonuclear flame subject to the Landau-Darrieus (L-D) instability [34] and $\dot{h}$ is the R-T growth rate described by (16), [2] with A and g depending on the radial location of the flame and the temporal expansion of the star. Equation (32) ought to provide slow initial burning with greater flame acceleration than steady state models in which

[2] We observe from the DNS that $u' \approx 1.2\dot{h}$; hence, (32) is consistent with Damköhler's flame speed model for large-scale turbulence [32, 20].

S_t is constrained by the transverse dimension of a computational test box [35] or the LES grid spacing [17].

The chief difficulty with (32) from a modeling standpoint is specifying the early-time growth of the R-T instability prior to attaining the fully turbulent regime; this will depend sensitively on the nature of the initial perturbations. Even if the overall flow is not particularly sensitive to details of the solution during the short transition period, this nascent stage sets the virtual starting length scale h_o in (17), which in turn determines the timing for the onset of rapid late-time growth ($t > \sqrt{h_o/\alpha g A}$). One could in principle derive h_o from the assumed initial state, e.g., from an initial spectrum of small-scale wrinkles generated by the L-D flame, or from a broader spectrum characteristic of turbulent thermal convection. Finally, effects of increasing Reynolds number could be introduced by adjusting the temporal dependence of α according to Fig. 6. Such a model would reflect the fact that the growth rate, mixing rate, kinetic energy content and interfacial surface area of the R-T turbulent region are all interrelated and all undergo a mild transition at $Re \approx 10^4$.

References and Notes

[1] Lord Rayleigh. Investigation of the character of the equilibrium of an incompressible heavy fluid of variable density. *Proc. Roy. Math. Soc.*, 14:170–177, 1883.

[2] G. I. Taylor. The instability of liquid surfaces when accelerated in a direction perpendicular to their plane. *Proc. Roy. Soc. London, Ser. A*, 201:192–196, 1950.

[3] S. Chandrasekhar. The character of the equilibrium of an incompressible heavy viscous fluid of variable density. *Proc. Camb. Phil. Soc.*, 51:162–178, 1955.

[4] E. Zweibel. Spinning a tangled web. *Nature*, 352:755–756, 1991.

[5] M. Versluis, B. Schmitz, A. von der Heydt, and D. Lohse. How snapping shrimp snap: Through cavitating bubbles. *Science*, 289:2114–2117, 2000.

[6] D. J. Stevenson. Light from tungsten on core construction. *Nature*, 378:763–764, 1995.

[7] A. N. Halliday. Mixing, volatile loss and compositional change during impact-driven accretion of the earth. *Nature*, 427:505–509, 2004.

[8] G. Bateman. *MHD Instabilities*. MIT Press, Cambridge, Massachusetts, and London, 1979.

[9] R. D. Petrasso. Rayleigh's challenge endures. *Nature*, 367:217–218, 1994.

[10] A. Burrows. Supernova explosions in the universe. *Nature*, 403:727–733, 2000.

[11] H. Lin, B. D. Storey, and A. J. Szeri. Rayleigh-Taylor instability of violently collapsing bubbles. *Phys. Fluids*, 14:2925–2928, 2002.

[12] R. P. Taleyarkhan, C. D. West, J. S. Cho, R. T. Lahey, Jr., R. I. Nigmatulin, and R. C. Block. Evidence for nuclear emissions during acoustic cavitation. *Science*, 295:1868–1873, 2002.

[13] M. Zingale, S. E. Woosley, C. A. Rendleman, M. S. Day, and J. B. Bell. Three-dimensional numerical simulations of Rayleigh-Taylor unstable flames in type Ia supernovae. *Astrophysical J.*, 632:1021–1034, 2005.

[14] J. P. Mellado, S. Sarkar, and Y. Zhou. Large-eddy simulation of Rayleigh-Taylor turbulence with compressible miscible fluids. *Phys. Fluids*, 17:Art. No. 076101, 2005.

[15] A. W. Cook and P. E. Dimotakis. Transition stages of Rayleigh-Taylor instability between miscible fluids. *J. Fluid Mech.*, 443:69–99, 2001.

[16] A. W. Cook, W. Cabot, and P. L. Miller. The mixing transition in Rayleigh-Taylor instability. *J. Fluid Mech.*, 511:333–362, 2004.

[17] V. N. Gamezo, A. M. Khokhlov, E. S. Oran, A. Y. Chtchelkanova, and R. O. Rosenberg. Thermonuclear supernovae: Simulations of the deflagration stage and their implications. *Science*, 299:77–81, 2003.

[18] R. E. Duff, F. H. Harlow, and C. W. Hirt. Effects of diffusion on interface instability between gases. *Phys. Fluids*, 5:417–425, 1962.

[19] F. X. Timmes and S. E. Woosley. The conductive propagation of nuclear flames. I. Degenerate C+O and O+Ne+Mg white dwarfs. *Astrophysical J.*, 396:649–667, 1992.

[20] N. Peters. *Turbulent Combustion*. Cambridge University Press, 2000.

[21] P. E. Dimotakis. The mixing transition in turbulence. *J. Fluid Mech.*, 409:69–97, 2000.

[22] A. W. Cook and Y. Zhou. Energy transfer in Rayleigh-Taylor instability. *Phys. Rev. E*, 66:art. no. 026312, 2002.

[23] J. R. Ristorcelli and T. T. Clark. Rayleigh-Taylor turbulence: Self-similar analysis and direct numerical simulations. *J. Fluid Mech.*, 507:213–253, 2004.

[24] H. Tennekes and J. L. Lumley. *A First Course in Turbulence*. MIT Press, Cambridge, 1972.

[25] G. Dimonte, D. L. Youngs, A. Dimits, S. Weber, M. Marinak, Wunsch S., C. Garasi, A. Robinson, M. J. Andrews, P. Ramaprabhu, A. C. Calder, B. Fryxell, J. Biello, L. Dursi, P. MacNeice, K. Olson, P. Ricker, R. Rosner, F. Timmes, H. Tufo, Y.-N. Young, and M. Zingale. A comparative study of the turbulent Rayleigh-Taylor instability using

high-resolution three-dimensional numerical simulations: The Alpha-Group collaboration. *Phys. Fluids*, 16:1668–1693, 2004.

[26] G. Dimonte, P. Ramaprabhu, D. L. Youngs, M. J. Andrews, and R. Rosner. Recent advances in the turbulent Rayleigh-Taylor instability. *Phys. Plasmas*, 12:056301, 2005.

[27] P. Ramaprabhu, G. Dimonte, and M. J. Andrews. A numerical study of the influence of initial perturbations on the turbulent Rayleigh-Taylor instability. *J. Fluid Mech.*, 536:285–319, 2005.

[28] S. E. Woosley, S. Wunsch, and M. Kuhlen. Carbon ignition in type Ia supernovae: An analytic model. *Astrophysical J.*, 607:921–930, 2004.

[29] K. Nomoto, K. Iwamoto, and N. Kishimoto. Type Ia supernovae; their origin and possible applications in cosmology. *Science*, 276:1378–1382, 1997.

[30] J. C. Niemeyer, W. K. Bushe, and G. R. Ruetsch. Approaches to modeling thermonuclear flames. In *Proceedings of the 1998 Summer Program*, pages 111–117. Center for Turbulence Research, 1998.

[31] M. Zingale, S. E. Woosley, J. B. Bell, M. S. Day, and C. A. Rendleman. The physics of flames in type Ia supernovae. In *Journal of Physics: Conference Series 16*, pages 405–409, 2005.

[32] G. Damköhler. Der einfluß der turbulenz auf die flammengeschwindigkeit in gasgemischen. *Z. Elektrochem.*, 46:601–652, 1940.

[33] W. Hillebrandt and J. C. Niemeyer. Type Ia supernova explosion models. *Annual Review of Astronomy and Astrophysics*, 38:191–230, 2000.

[34] F. K. Röpke, J. C. Niemeyer, and W. Hillebrandt. On the small-scale stability of thermonuclear flames in type Ia supernovae. *Astrophysical J.*, 588:952–961, 2003.

[35] A M. Khokhlov, E. S. Oran, and J. C. Wheeler. Scaling in buoyancy-driven turbulent premixed flames. *Combust. Flame*, 105:28–34, 1996.

Acknowledgments

We wish to thank H. R. Childs for his assistance in creating figures 1 and 10. This work was performed under the auspices of the U.S. Department of Energy by the University of California Lawrence Livermore National Laboratory under contract No. W-7405-Eng-48.

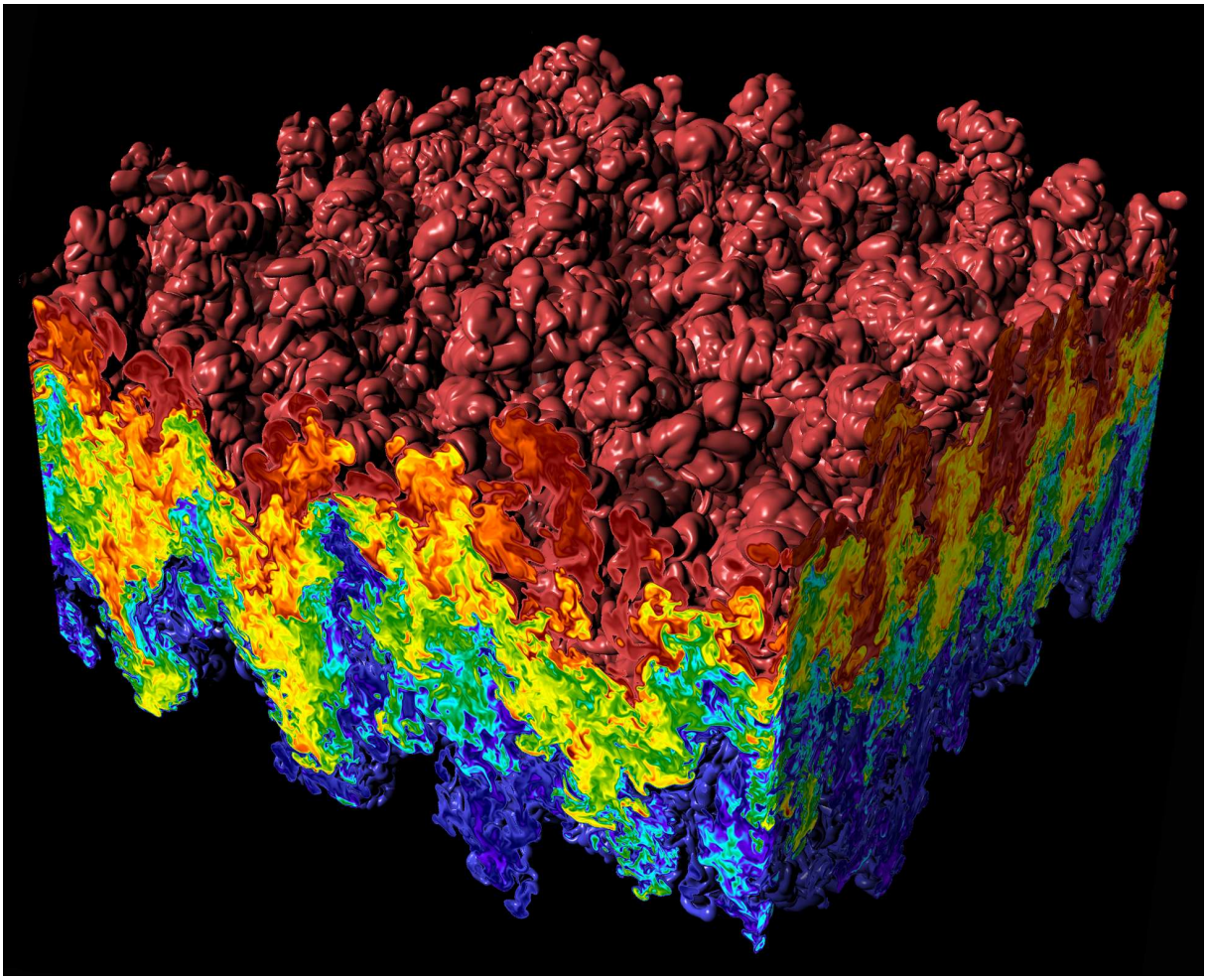

Figure 1: Rayleigh-Taylor instability in the fully turbulent regime at $t/\tau = 28$. Blue fluid is light (density=1) and red fluid is heavy (density=3).

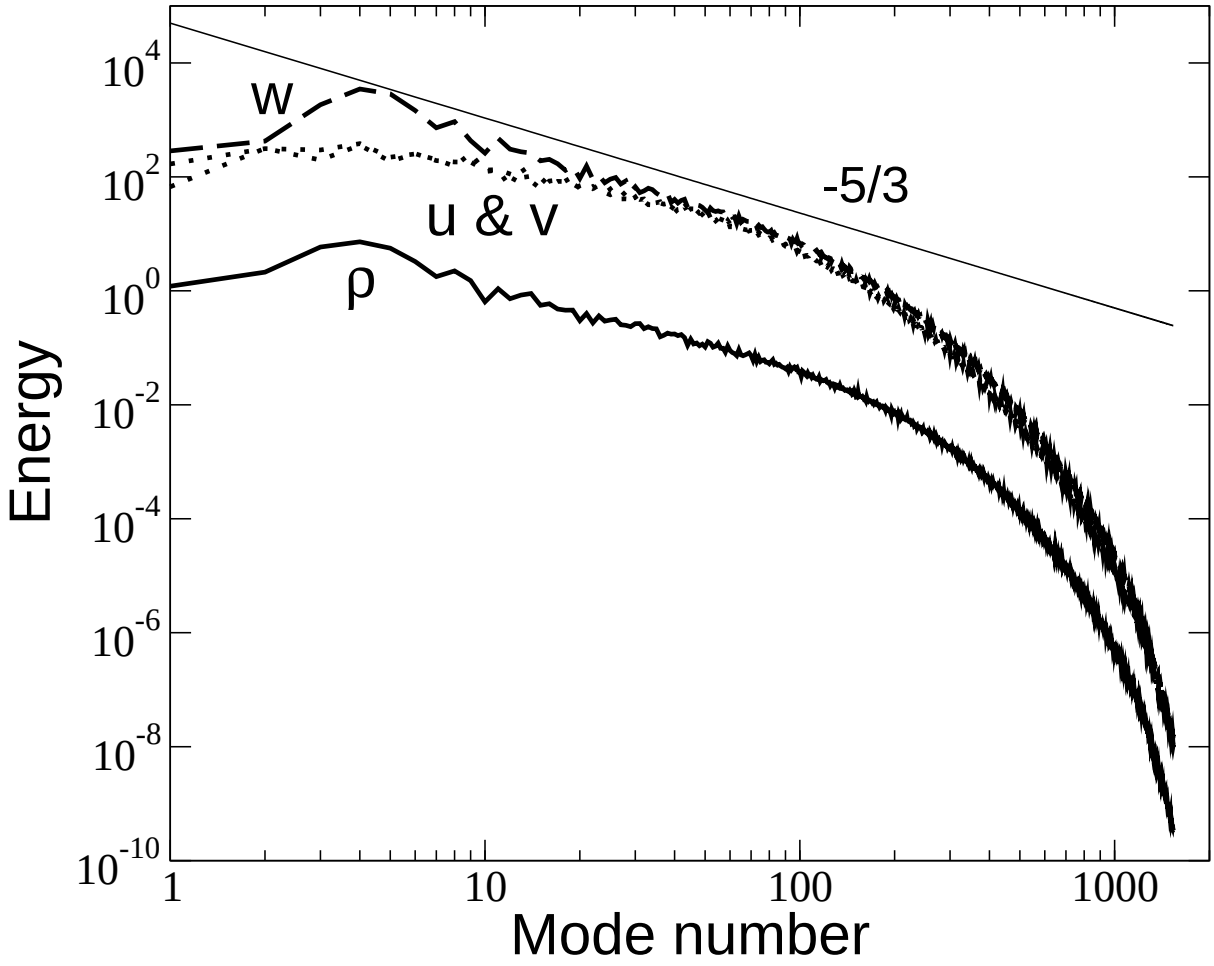

Figure 2: Energy spectra of density and velocity components in the $z = 0$ plane at $t/\tau = 31$. The mode number is $kL/2\pi$, where k is the wavenumber and L is the size of the numerical domain in the horizontal directions. A fiducial corresponding to Kolmogorov scaling ($k^{-5/3}$) is drawn for reference.

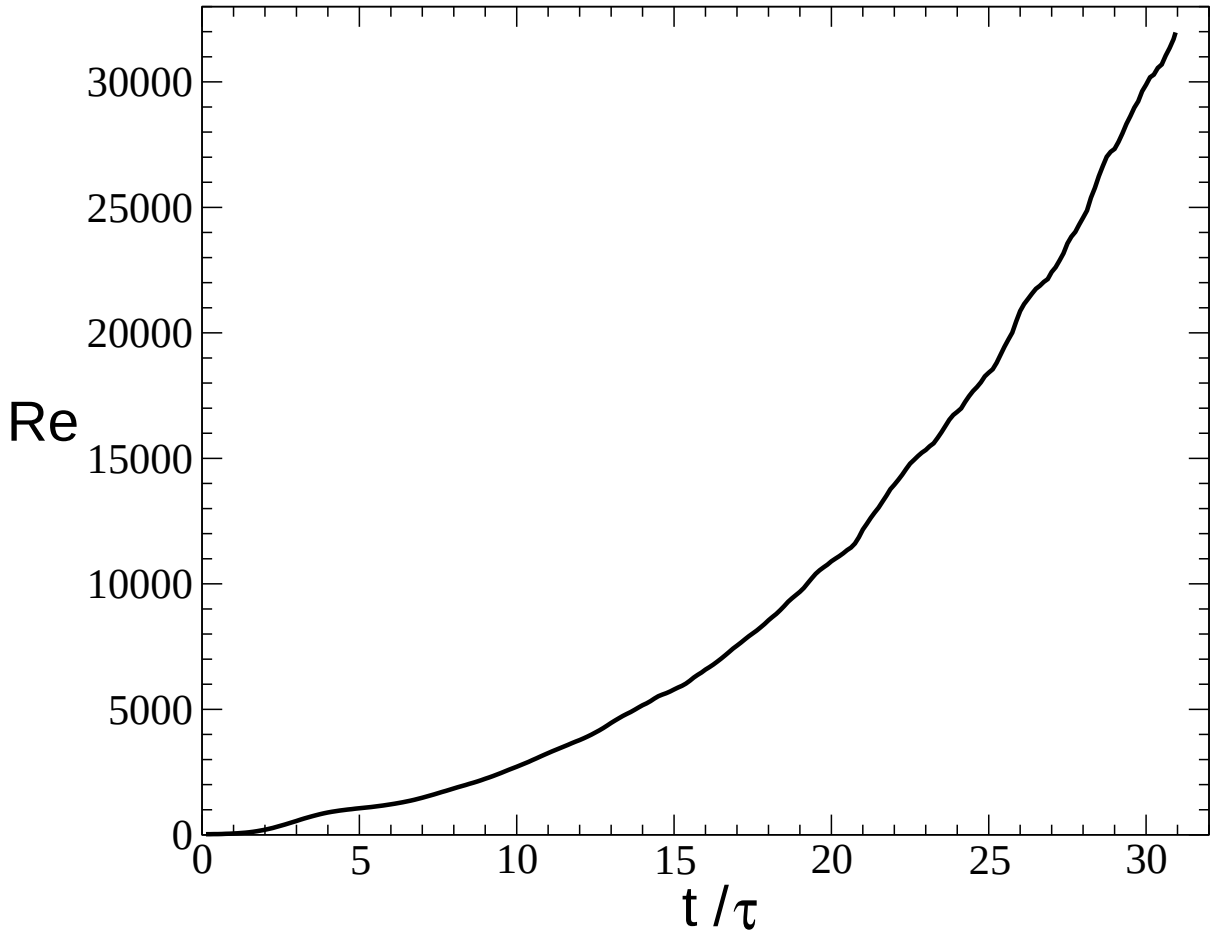

Figure 3: DNS Reynolds number of R-T instability. Here $Re \equiv H\dot{H}/\nu$, where H is the range in z for which $0.01 \leq \langle X \rangle \leq 0.99$, where X is the mole fraction of heavy fluid (7).

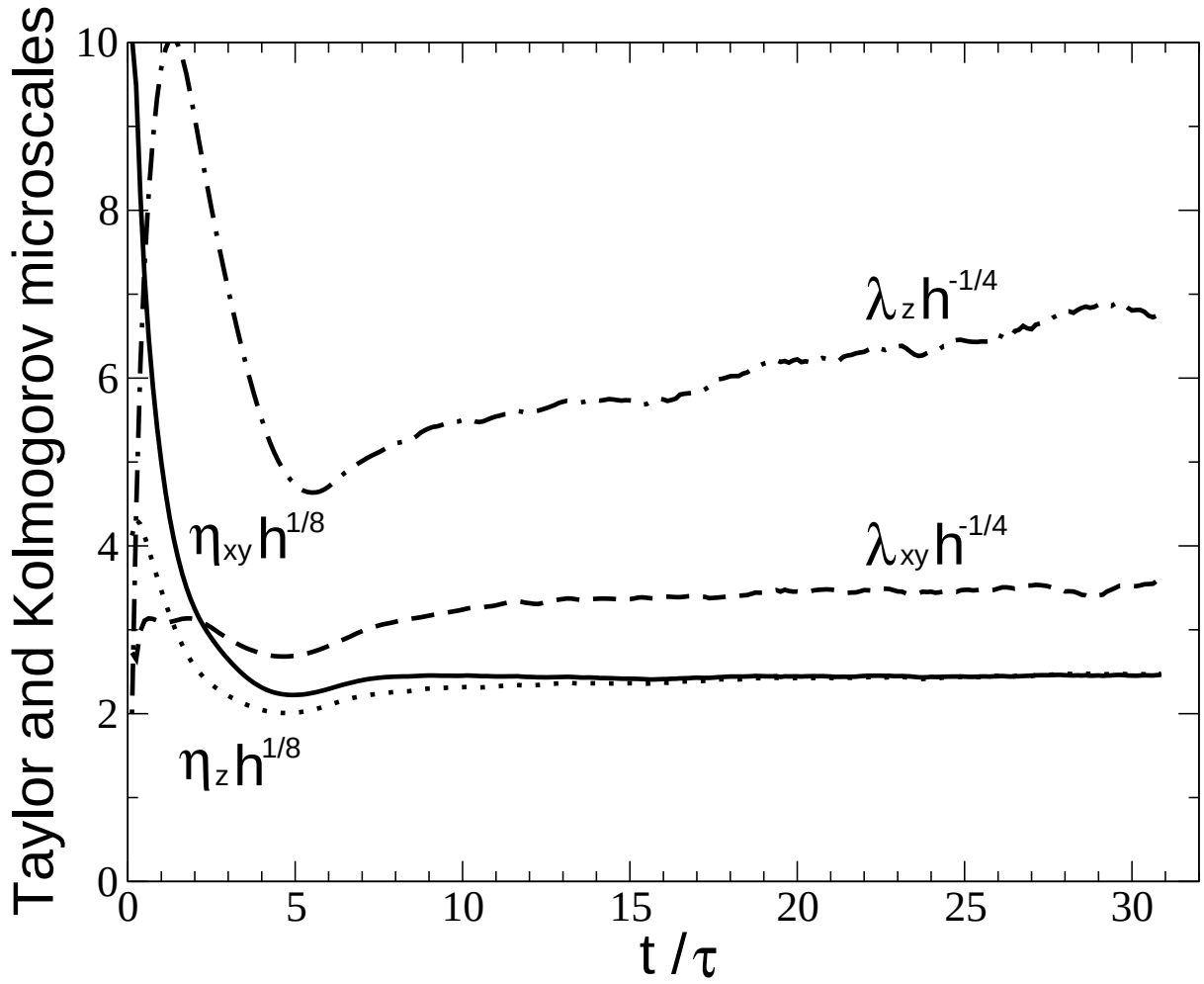

Figure 4: Scaled Taylor microscales, λ_i, and Kolmogorov scales, η_i, on the $z = 0$ plane.

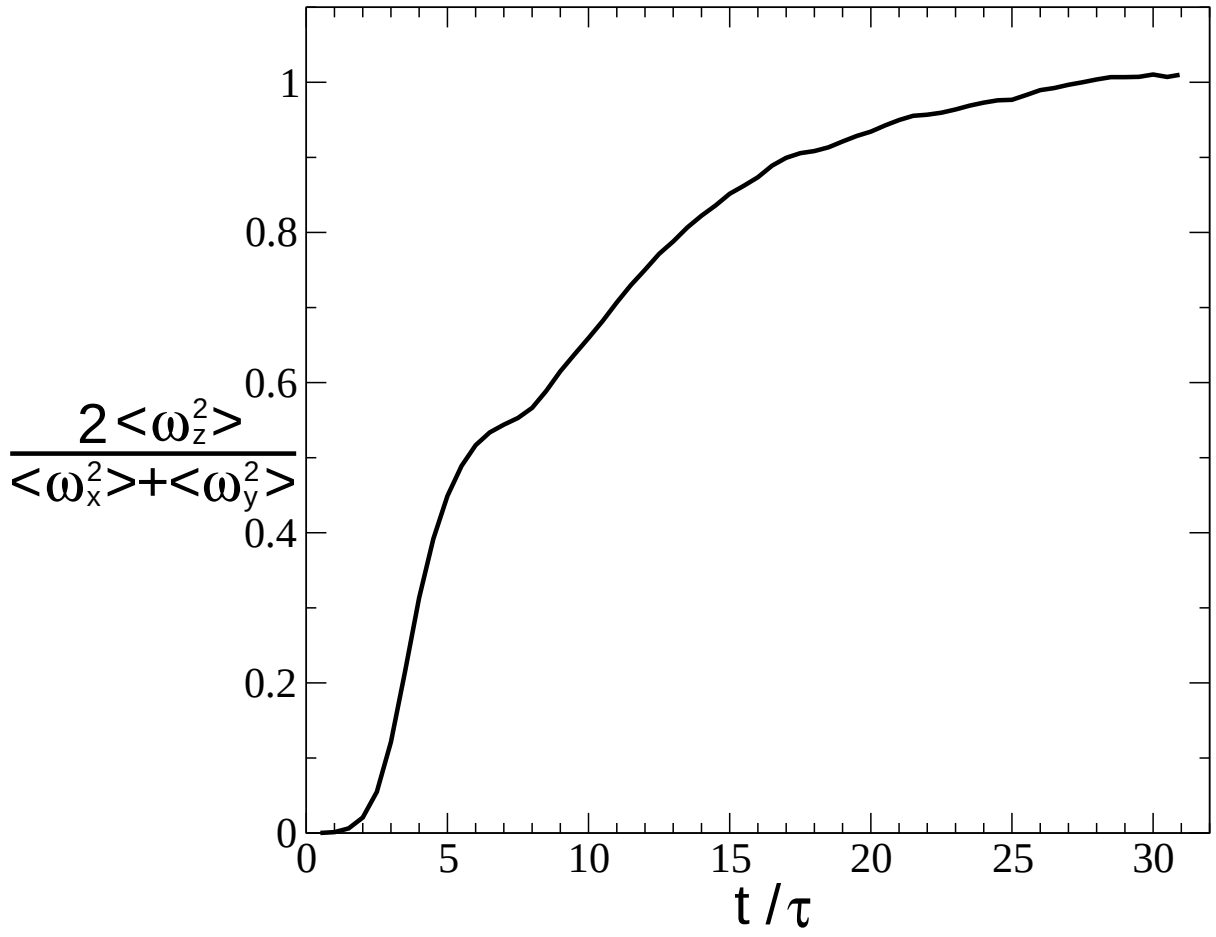

Figure 5: Isotropy of vorticity ($\boldsymbol{\omega} \equiv \nabla \times \mathbf{u}$) in the region $-h/3 \leq z \leq h/3$. Zero corresponds to complete anisotropy, and unity corresponds to complete isotropy.

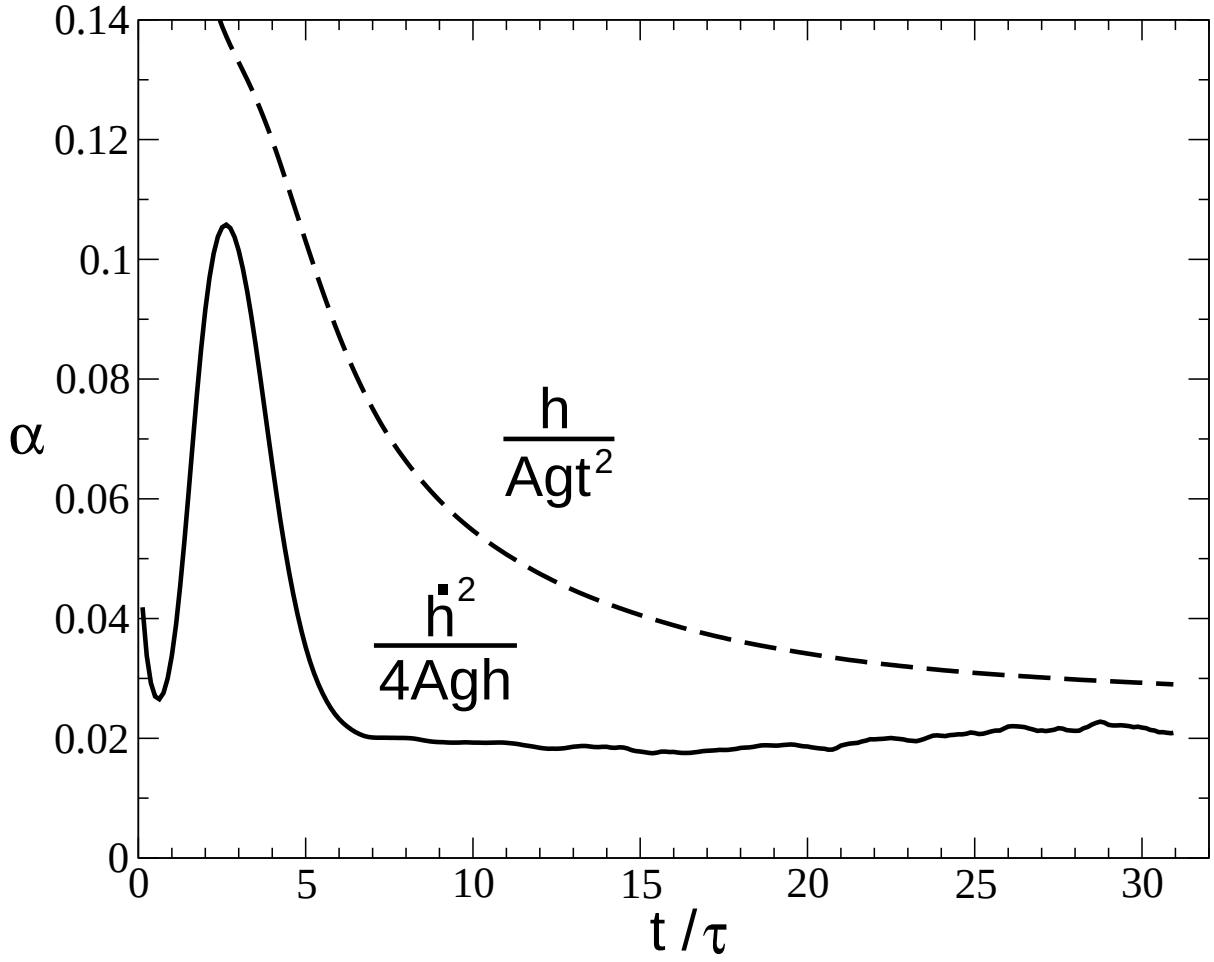

Figure 6: Growth constant determined by the most common method (dashed line) and by the similarity method (solid line).

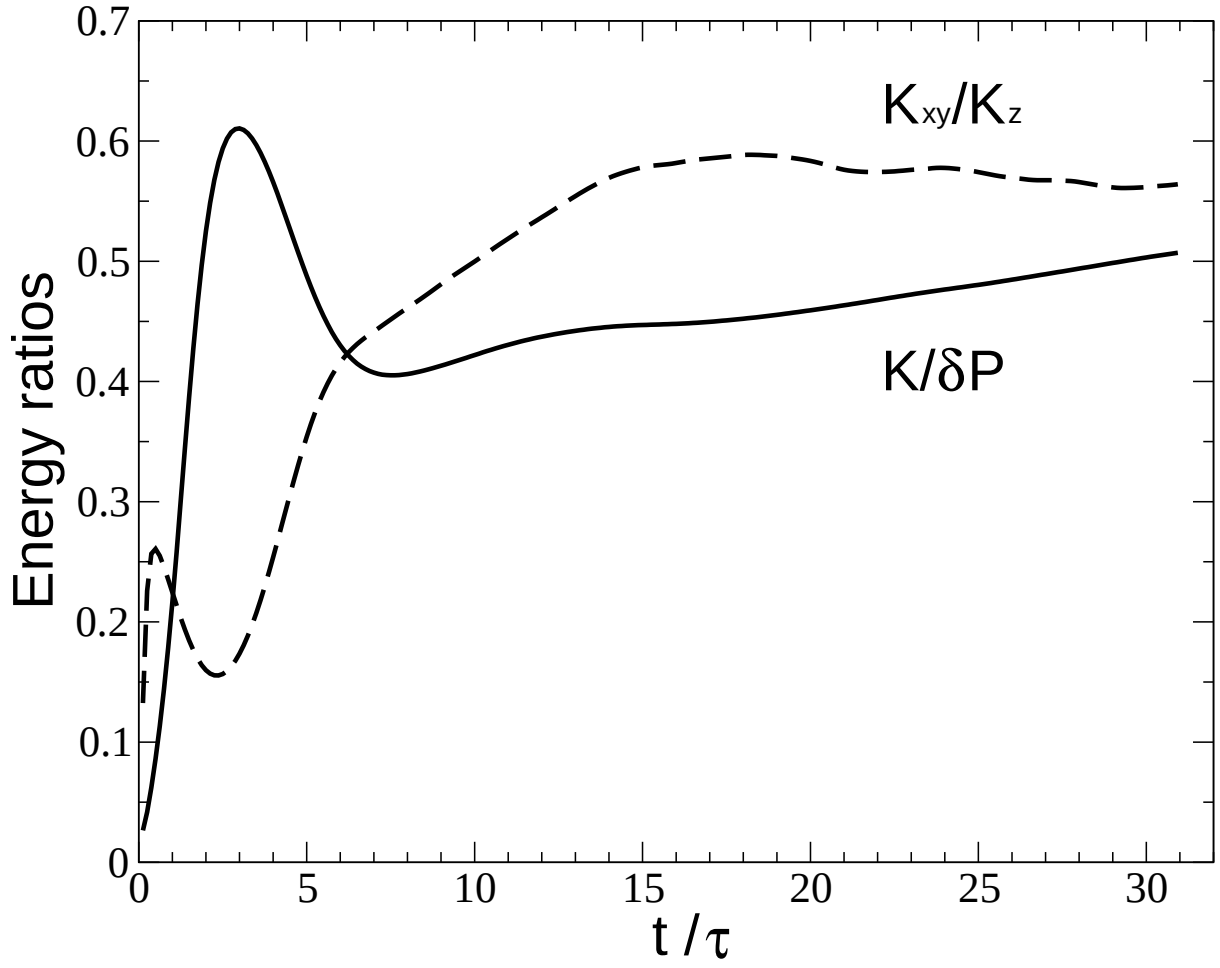

Figure 7: Ratios of total kinetic energy to released potential energy, and horizontal kinetic energy to vertical kinetic energy.

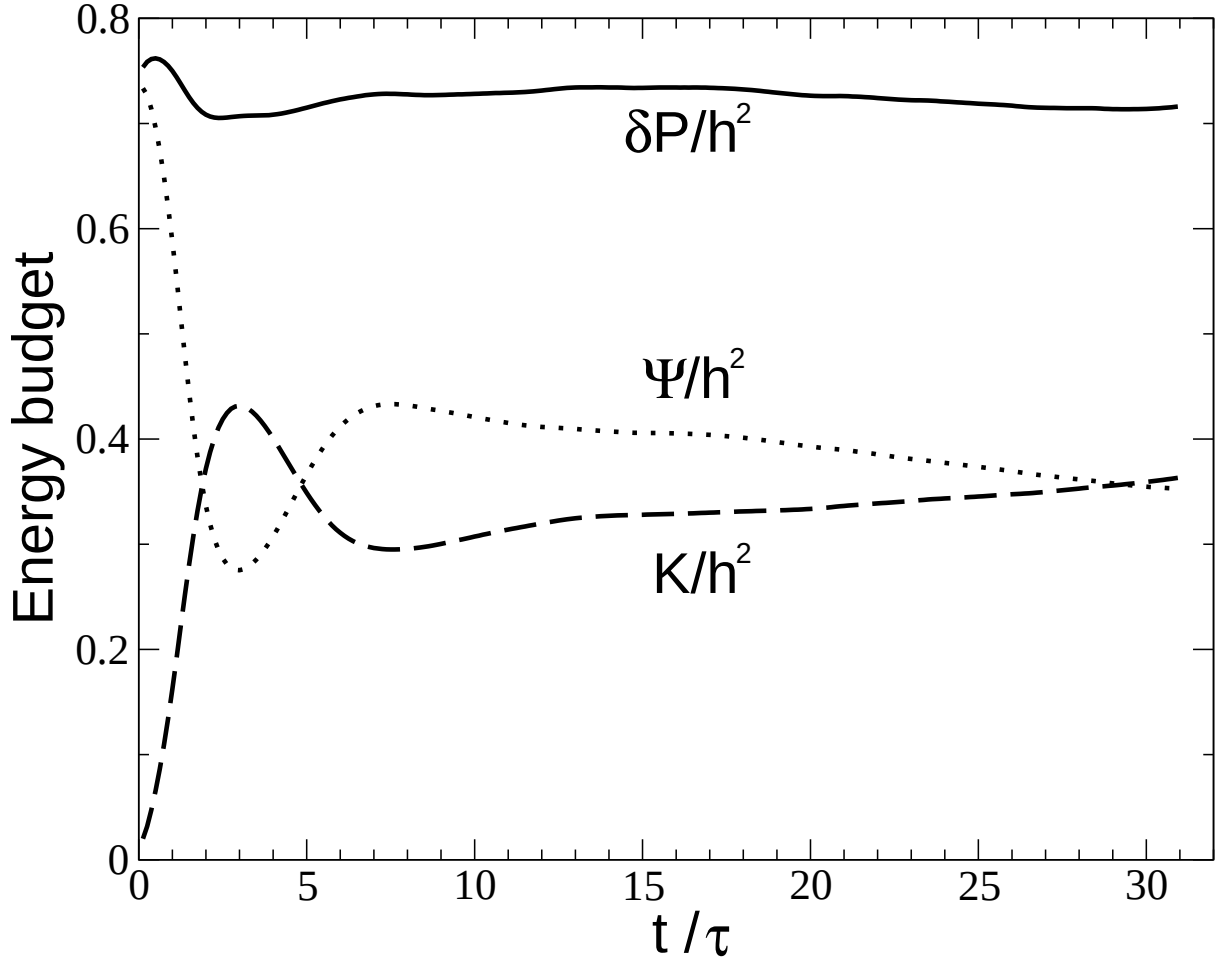

Figure 8: Released potential energy (δP), total kinetic energy (K) and total dissipated energy (Ψ) normalized by h^2.

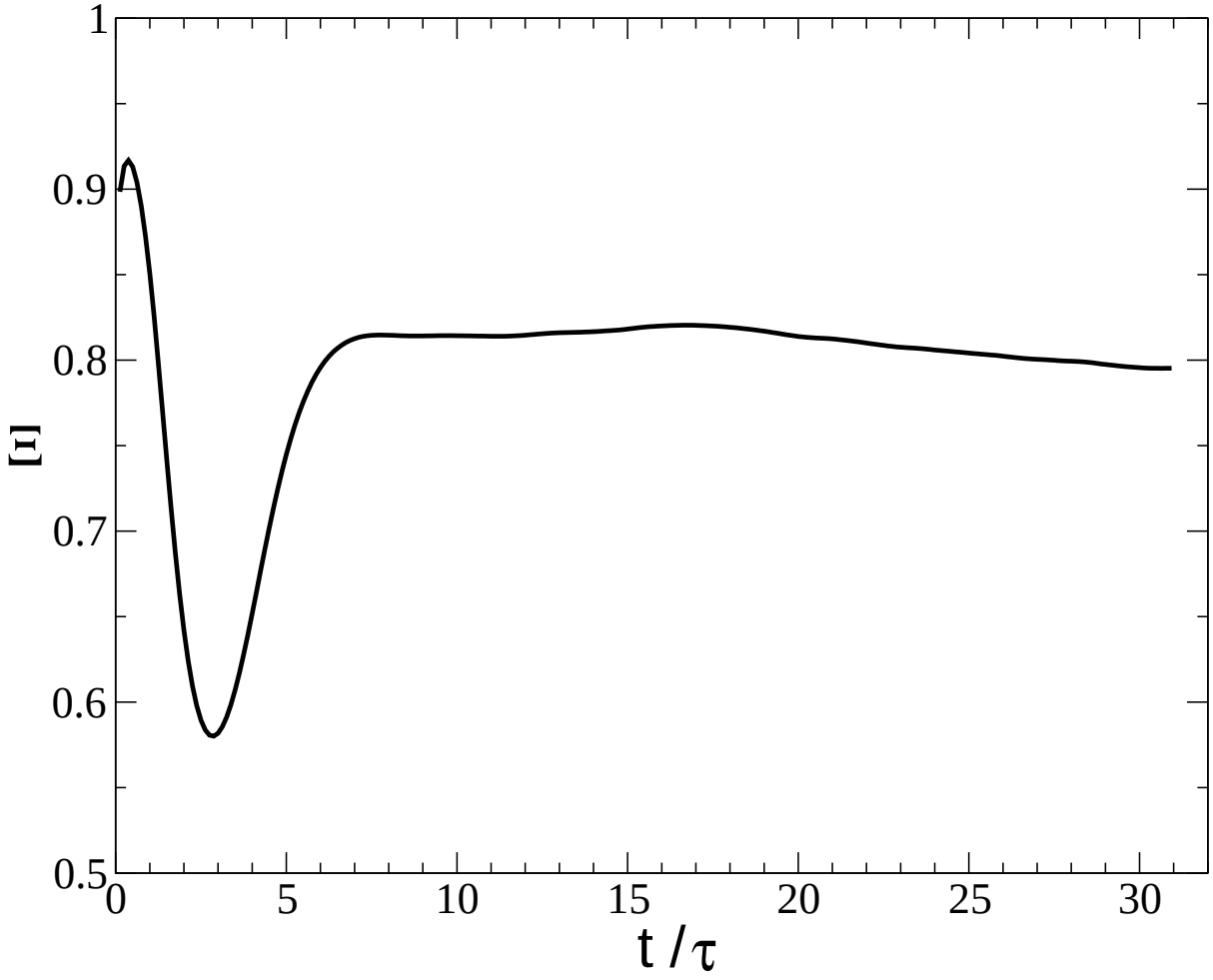

Figure 9: Ratio of mixed to entrained fluids. Zero corresponds to complete segregation within the layer (immiscible), and unity corresponds to complete homogenization.

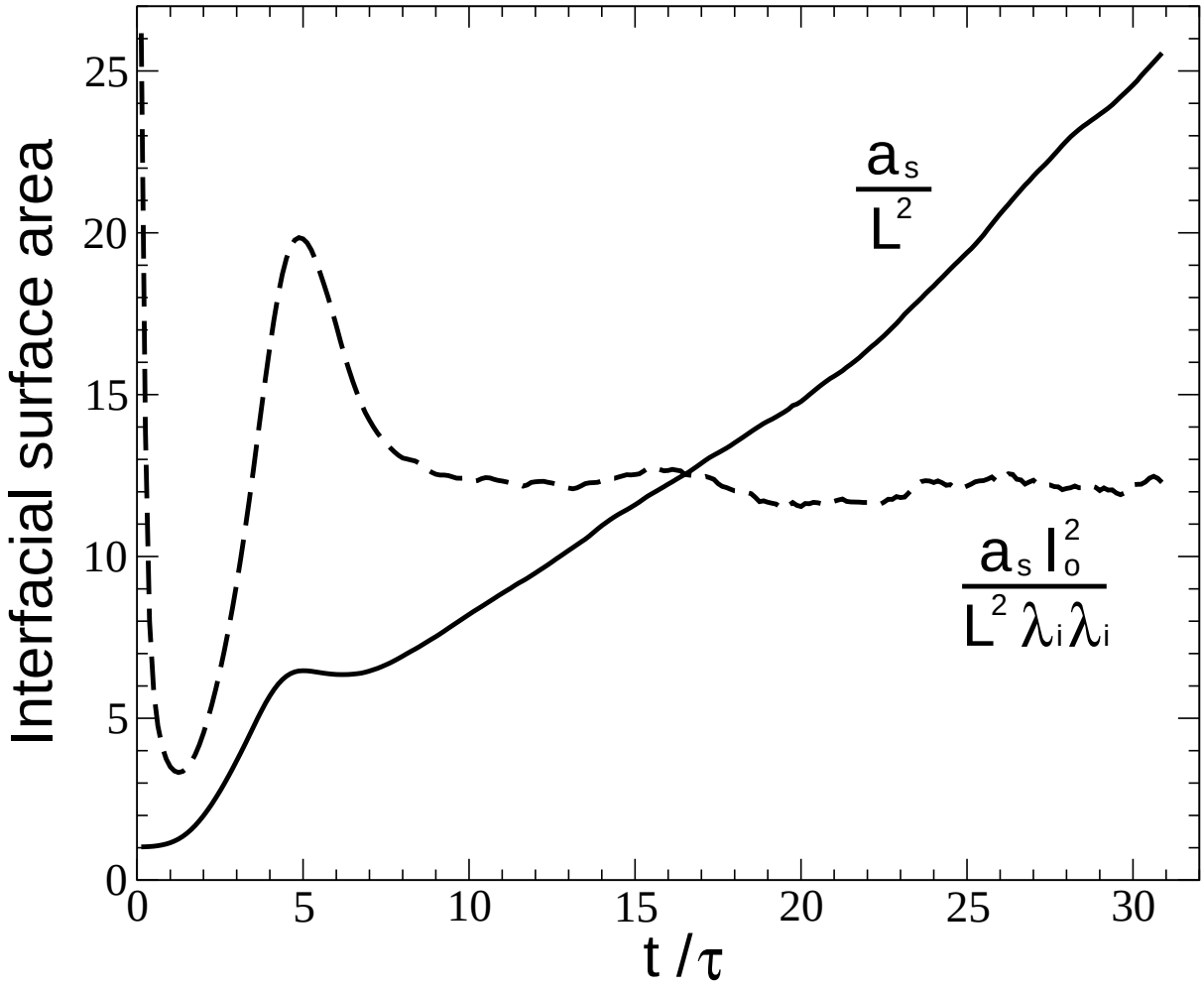

Figure 10: Normalized area of equimolar $(X = 1/2)$ surface.